Collision-induced intramultiplet mixing for $Ne^{**}\{(2p)^5(3p)\}+He$: Experiments and quantum calculations

M. P. I. Manders, J. P. J. Driessen, H. C. W. Beijerinck, and B. J. Verhaar
Physics Department, Eindhoven University of Technology, Postbox 513, NL-5600 MB Eindhoven, The Netherlands
(Received 21 September 1987)

We have investigated fine-structure–changing collisions of short-lived (20-ns) Ne^{**} atoms in the $\{\alpha\}\equiv\{(2p)^5(3p)\}$ multiplet with ground-state He atoms. A newly designed cross-beam apparatus allows the measurement of accurate polarized cross sections $Q_{l\leftarrow k}^{|M_k|}$ for the $\{\alpha\}_k\rightarrow\{\alpha\}_l$ transition. In the experiment, the initial $\{\alpha\}_k$ state is prepared with a well-defined asymptotic orientation M_k of its electronic angular momentum **J**, through excitation of metastable Ne^* atoms with a polarized laser. The reported transitions are mainly between states in the $\{\alpha\}_{4,5,6,7}$ group (Paschen numbering), at approximately 100 meV center-of-mass energy. Some of these exhibit very strong polarization effects, with differences between $Q_{l\leftarrow k}^{|M_k|}$ and $Q_{l\leftarrow k}^{|M_k'|}$ of up to a factor 4. Fully quantum-mechanical coupled-channel calculations on a diabatic basis, with the Ne^{**}-He model potentials of Hennecart and Masnou-Seeuws as input, prove successful in reproducing experimental results. Cross-section behavior may be qualitatively understood from the presence of avoided crossings between the adiabatic potentials, indicative of strong radial coupling. The restraint of reflection symmetry is strongly felt here. In addition, the effects of rotational coupling can be readily identified.

I. INTRODUCTION

Inelastic collisions of atoms in short-lived, electronically excited states presently are the focus of attention of both theorists[1–4] and experimentalists.[5–17] A recent review of the field has been given by Hertel *et al.*[18] The dependence of the outcome of the collision process on the initial orientation of the electronic angular momentum with respect to the initial relative velocity of the collision partners has proven to reveal many interesting features of the potential surfaces and collision dynamics.[2,6,7] So far, most experiments have been performed in bulk. Only recently, crossed-beam experiments with a much better defined initial relative velocity have been reported,[6,7] resulting in more reliable results on these polarization effects. Until now, the rather simple one-electron alkali-metal[4–6,12–14] and two-electron alkaline-earth[3,7–9,15] systems have received most attention, with less emphasis being put on noble gas atoms.[16,17]

In this paper we report the first crossed-beam study of inelastic, fine-structure–changing collisions for the system

$$Ne^{**}[\{(2p)^5(3p)\}_k;J_k]+He\rightarrow Ne^{**}[\{(2p)^5(3p)\}_l;J_l]+He+\Delta E_{k,l} \quad (1)$$

involving beams that are well characterized with respect to direction, velocity, and excited-state polarization. Strong, interesting polarization effects have been observed and absolute values of cross sections have been determined with a high accuracy of 25%. We have touched upon this subject already in an earlier Letter.[19] In a study of this sort, He is a "natural" choice as a collision partner for the short-lived Ne^{**} atoms. Some of the reasons for this may be deduced from the energy-level scheme in Fig. 1, which shows the first- and second-excited multiplets, plus the ionization limit, of the rare-gas atoms from He to Xe. It will be apparent that, at other than very high energies, a collision partner of either lighter or equal mass precludes the possibility of processes like Penning ionization or excitation transfer obscuring the intramultiplet mixing picture. So, for $Ne^{**}+He$ (and $Ne^{**}+Ne$), the ground-state atom can be assumed to remain in the ground state. Likewise, there will be no chance of other than the short-lived Ne^{**} states playing a part.

Typical lifetimes of the $\{\alpha\}_i\equiv\{(2p)^5(3p)\}_i$ states, with i running from 1 to 10 with decreasing energy, are $\tau\approx 20$ ns. The total energy spread of the multiplet is $\Delta E_{1,10}=584$ meV. The Ne states are shown in Fig. 2. Although a large number $\sum_{i=1}^{10}(J_i+1)=23$ of molecular states is involved, which complicates the analysis of the observed transitions, the Ne^{**}-He system has two major advantages, besides the ones already cited. Firstly, the process of intramultiplet mixing has been investigated in detail in the afterglow of gas discharges, resulting in a suitable set of reference rate constants for Ne and He as collision partners.[11,20–23] Secondly, model potentials are available for the Ne^{**}-He system,[1] allowing a direct comparison of theory and experiment by means of fully quantum-mechanical coupled-channel calculations. In the Ne^{**}-Ne case such a calculation is complicated by

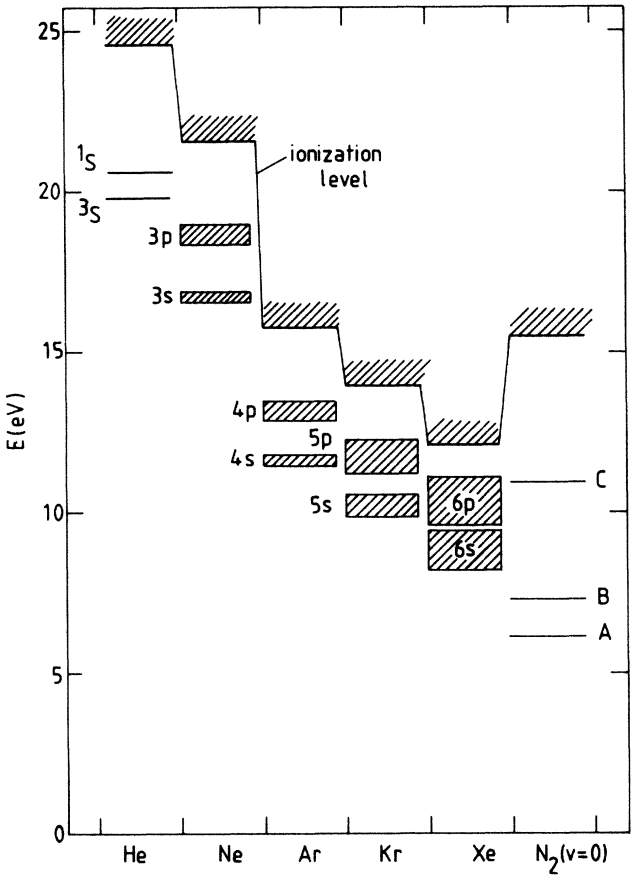

FIG. 1. Energy levels of the rare gases from He through Xe, plus N_2 as a typical molecule. Indicated are the first (ns) and second (np) excited multiplets, as well as the ionization limit.

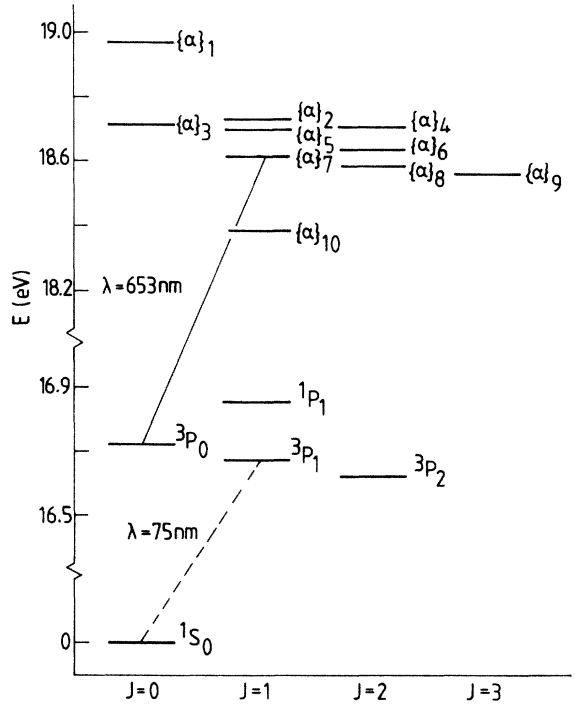

FIG. 2. Energy-level diagram of the $Ne^*\{(2p)^5(3s)\}$ (Russell-Saunders notation) and $Ne^{**}\{(2p)^5(3p)\} \equiv \{\alpha\}$ (Paschen numbering) excited states, grouped by their electronic angular momentum quantum number J.

the presence of additional symmetries, due to equal charges for $^{22}Ne^{**}$-^{20}Ne, and to both equal charges and identical particles for $^{20}Ne^{**}$-^{20}Ne. For the present paper we limit our discussion to the Ne^{**}-He case.

II. COLLISION DYNAMICS

A. Scattering process

The Hamiltonian governing the process of Eq. (1) consists of the kinetic energy operator of nuclear motion T_n, with radial and rotational components T_{rad} and T_{rot}, and the electronic molecular Hamiltonian H^{mol}, which contains the atomic Hamiltonians $H^{Ne^{**}}$ and H^{He} as well as the molecular interaction $V^{Ne^{**}\text{-He}}$:

$$H = T_{\text{rad}} + T_{\text{rot}} + H^{Ne^{**}} + H^{He} + V^{Ne^{**}\text{-He}} . \quad (2)$$

The relative motion of the nuclei results in a rotational angular momentum **N**. At the same time, both the Ne^{**} atom and its collision partner may in principle possess an intrinsic angular momentum **J**. In fact, as we have seen, the He atom remains in the ground state, and we will at all times have total electronic angular momentum $\mathbf{J} = \mathbf{J}_{Ne^{**}}$. Electronic and rotational angular momentum couple to total angular momentum $\mathbf{P} = \mathbf{N} + \mathbf{J}$, which is a conserved quantity. The initial and final Ne^{**} atomic states may have different **J**. Within the limits posed by $\mathbf{P} = \mathbf{N} + \mathbf{J}$, N will change accordingly. Due to inversion symmetry, the total parity π is a conserved quantity as well.

At the present collision energies of less than 0.5 eV, relative velocities of the colliding atoms are small compared to electron velocities. Consequently, the electronic wave function will be able to adapt itself more or less adiabatically to the orientation of the internuclear axis. The picture that thus emerges is that of a quasimolecular system. The interaction between the collision partners is apt to be governed by the molecular potential curves. However, other than in the completely adiabatic Born-Oppenheimer approach, the molecular states are still coupled by the nuclear motion.

It is apparent from the above that the molecular quantum number $\Omega = |M_{J_{z'}}|$, with $M_{J_{z'}}$ the magnetic quantum number with respect to the body-fixed internuclear axis **z'**, will have relevance at small distances. We note that the $J_{z'}$ operator does not commute with **N**, so that a description in terms of the quantum number N of nuclear rotational motion then becomes infeasible. Naturally, the above adiabatic, i.e., molecular, picture does not rule out a description in diabatic, i.e., atomic, terms, as long as a sufficient number of basis states are included in either description. Indeed, atomic terms are naturally associated with the asymptotic state of the system, which ultimately decides the outcome of the scattering experiment.

B. Model potential method for Ne^{**}-He

The atoms in our collision experiment constitute a quasimolecular system. The experiment may be interpreted through the relevant molecular potential curves,

i.e., eigenvalues of the molecular Hamiltonian H^{mol}. With regard to these, *ab initio*[24] and configuration-interaction[25] calculations for the Ne*-Ne system have met with limited success. For the case of the Na-Ne interaction, the model potential method, which solves a one-electron Schrödinger equation for the motion of the valence electron in the effective potential of the two cores, gives fairly accurate results.[26]

To extend the model potential method to the Ne**-rare gas systems, the coupling of angular momentum (orbital and spin) of the $(3p)$ valence electron and the $(2p)^{-1}$ open shell core has to be included, and may be expected to have considerable effect.[27] The definition of an effective potential takes proportionally more effort. This problem has been solved by Hennecart and Masnou-Seeuws[1] and Hennecart[11] for Ne**-He at internuclear distances $R \geq 4.5a_0$, using an iterative, first-order perturbation treatment. For a start, they solve the one-electron problem for an effective zero-order molecular interaction potential V_{int} that contains only the spherical part H_a of the atomic electron-core interaction, as well as the molecular electron-He and electron-core-He interactions. This results in eigenvalues $V_\sigma(R)$ and $V_\pi(R)$ for the $(3p)$, $|m_l|=0$ and $(3p)$, $|m_l|=1$ molecular states, respectively, with m_l the magnetic subquantum number for the orbital angular momentum of the valence electron. Comparison of calculated atomic and molecular electron orbitals indicates that the $(2p)^{-1}$ core orbital is not modified by the presence of the perturbing rare gas atom and that the modification of the $(3s)$ and $(3p)$ valence-electron wave functions is limited to a small region around the perturber. For internuclear distances $R \geq 4.5a_0$, which is the lower limit of the $V_\sigma(R)$ and $V_\pi(R)$ calculation by Hennecart and Masnou-Seeuws, this places the modification well outside the core region.

The spin-orbit coupling and the nonspherical part of the electron-core interaction can thus be calculated by first-order perturbation theory in an atomic $|LSJM_J\rangle$ basis, with L,S, and J the orbital, spin, and total Ne angular momentum quantum numbers. In the same $|LSJM_J\rangle$ basis, the matrix elements of V_{int} have been calculated by Hennecart and Masnou-Seeuws[1] and Hennecart[11] through the method of representing V_{int} in terms of irreducible tensor operators. The matrix elements are given by linear combinations of $V_\sigma(R)$ and $V_\pi(R)$.

Hennecart and Masnou-Seeuws then assume a diagonal charge-induced dipole core-He interaction $V^{\text{core}}(R) = -C_4/R^4$. Thereby the electronic Hamiltonian H^{mol} for $R \geq 4.5a_0$ is completely determined. With the expansion of the $\{\alpha\}_k$ atomic states in the $|LSJM_J\rangle$-basis known, H^{mol} may be transformed to the $|\alpha JM_J\rangle$ representation. Diagonalization yields the molecular, adiabatic, eigenstates $|\alpha J\Omega(R)\rangle$ and potential curves $V_k^\Omega(R)$. The 23 adiabatic potential curves are, of course, divided into Ω manifolds. Additionally, for $\Omega=0$ the constraint of reflection symmetry generates distinct + and − classes, containing the even and odd J states, respectively.

The above potentials, given for $R \geq 4.5a_0$, can only be used as input for a full coupled-channel calculation through the addition of a hard wall at the cutoff distance. In the case of an adiabatic potential curve of a repulsive nature, this is a reasonable assumption, especially at low energies. For the curves which are attractive at $R = 4.5a_0$, this procedure is more debatable. To investigate the importance of the inner potential regions for the calculated inelastic cross sections, we have extended the potentials to smaller distances. This was done both for the valence electron-He interaction (in a simple empirical way) and for the core-He interaction.

We first consider the general character of the valence-electron and core potentials at small distances. As was the case for the valence electron, different core orientations will result in different core-He potentials: $V_\sigma^{\text{core}}(R)$ and $V_\pi^{\text{core}}(R)$ for the $(2p)^{-1}$, $|m_l|=0$ and $(2p)^{-1}$, $|m_l|=1$ molecular states (see Fig. 3). For the $(3p)$ valence electron, the repulsive forces arising from the overlap of wave functions will be more important at a given separation for the σ state than for the π state, due to the σ-wave function being oriented towards the ground-state atom. For the $(2p)^{-1}$ core hole this situation is reversed: The π potential will be more repulsive than the σ potential. Moreover, due to the smaller spatial extension of the $(2p)^{-1}$ wave function, the corresponding repulsive forces will be of shorter range. At large distances, where the weakly attractive dispersion interaction becomes dominant, V_σ will be slightly more attractive than V_π, due to the greater polarizability of the σ orbital. At these distances, any effect of the core orientation will be negligible. The potentials of Hennecart and Masnou-Seeuws for the valence electron, given for $4.5a_0 \leq R \leq 15a_0$, indeed display the expected short-range behavior, while V_σ is still slightly repulsive at $R = 15a_0$.

The extension of the V_π and V_σ valence-electron potentials was performed in the following way. To V_σ we added a repulsive exponential core; V_π was extrapolated on the basis of an electrostatical model for the contribution of the two lobes of the π orbital to the charge-

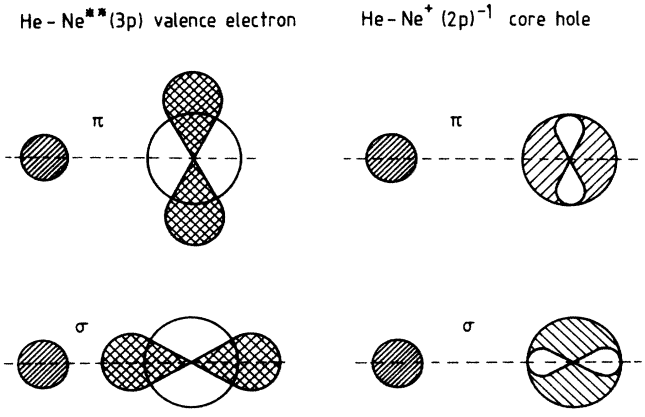

FIG. 3. Ne $(3p)$ valence electron (cross-hatched) and $(2p)$ core hole (hatched) charge distributions associated with the π and σ states of the e^--He and Ne^+-He systems. The attractive-repulsive character of the valence electron π- and σ-orientation potentials is reversed in the case of the core hole.

induced dipole electron-He interaction. The core-He potential[28] may be derived from the spectroscopy of the $(NeHe)^+$ ion.[29] From a certain internuclear distance $R \geq 6a_0$, it equals the diagonal charge-induced dipole core-He interaction $-C_4/R^4$, mentioned earlier. Apart from an additional phase factor $(-1)^{L-L'}$, the V_σ^{core} and V_π^{core} contributions to the Ne**-He interaction matrix in the $|LSJM_J\rangle$ representation can be calculated in the same way as the V_σ and V_π valence-electron contributions, i.e., by using the formalism of irreducible tensor operators. The potentials resulting from this approach are shown in Fig. 4 (for $R < 4.5a_0$), together with the original potentials of Hennecart and Masnou-Seeuws (for $R \geq 4.5a_0$). We observe that the general behavior of the various potentials is in agreement with our discussion of the different character of the σ and π states of the valence electron and the core hole.

In Fig. 5 we show some adiabatic potential curves $V_k^\Omega(R)$ of relevance to this paper. They were calculated from the potentials of Fig. 4. The states $\{\alpha\}_k$ with $k = 4,5,6,7$ that appear in Fig. 5 form a multiplet of special interest, on account of the presence of a number of unmistakable avoided crossings between their adiabatic potentials. It is important to note that only at fairly small internuclear distances the Ω splitting $V_k^\Omega - V_k^{\Omega'}$ between the potential curves for a given $\{\alpha\}_k$ state grows large, compared to the rotational coupling strength. Therefore, at larger distances, there will be no "locking" of the electronic angular momentum J to the internuclear axis, i.e., no Ω conservation.

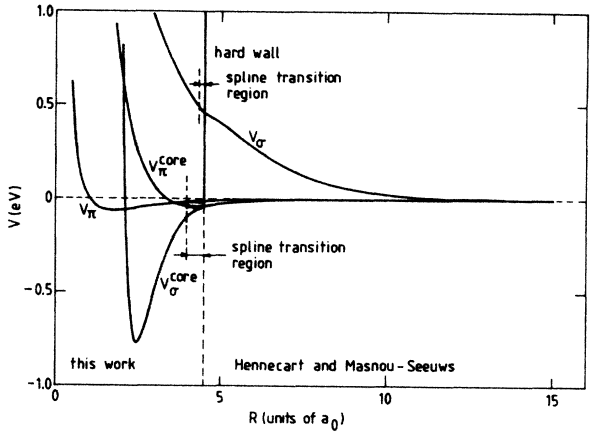

FIG. 4. Potentials resulting from the e^--He and Ne^+-He interaction for the π and σ orientations. For internuclear distances $R > 4.5a_0$, these follow the prescription of Hennecart and Masnou-Seeuws. At smaller distances they result from the extension procedure described in Sec. II B. In each case the cubic spline transition region has been indicated.

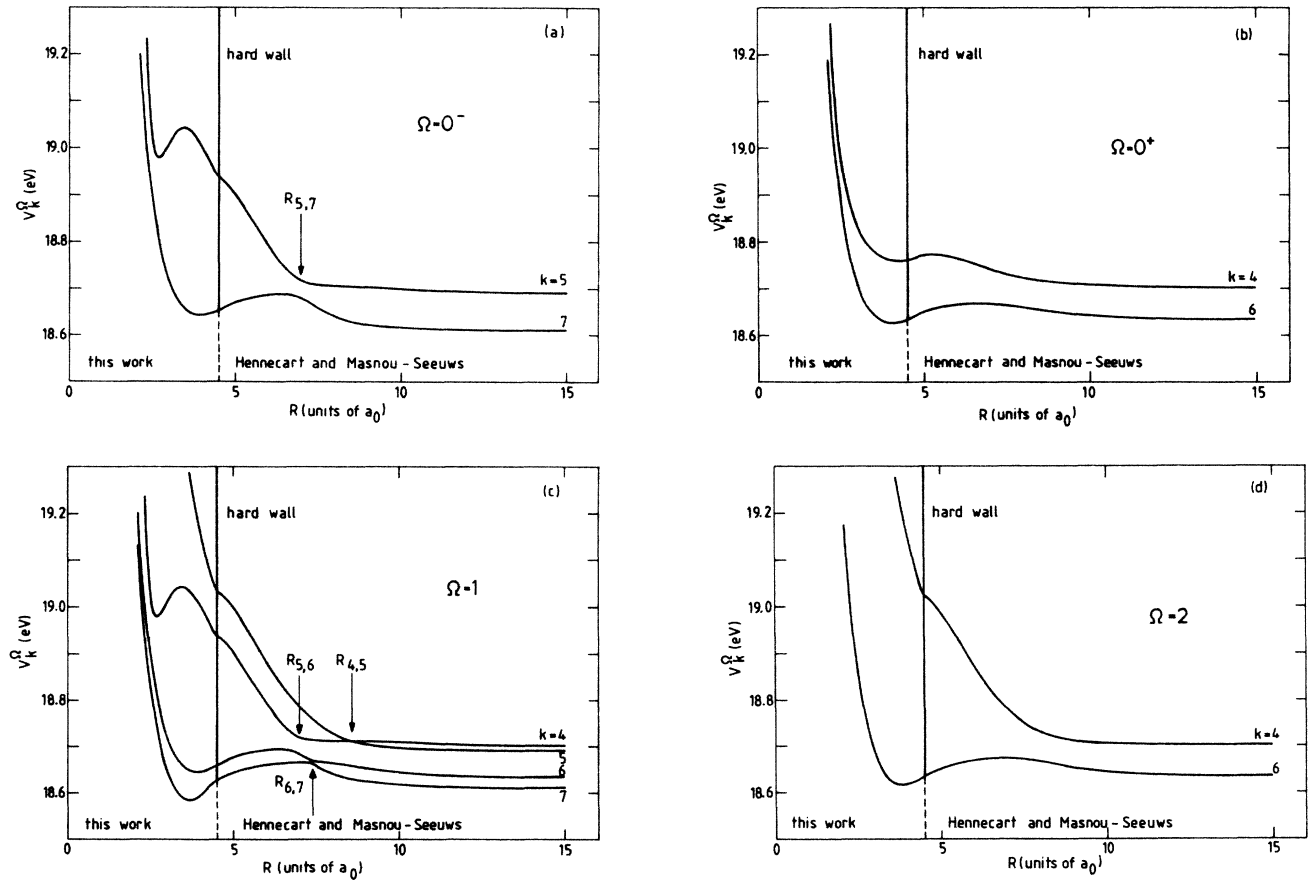

FIG. 5. Adiabatic potential curves $V_k^\Omega(R)$ for the $\{\alpha\}_{k=4,5,6,7}$ multiplet of special interest, as derived from the basic potentials of Fig. 4. The arrows point to the position $R_{k,l}$ of unmistakable avoided crossings.

III. COUPLED-CHANNEL CALCULATION

A. Coupled-channel theory

The stationary state Ne**-He wave function $\psi(\mathbf{r},\mathbf{R})$, where $\mathbf{r}$ represents all electron coordinates and $\mathbf{R}$ is the internuclear radius vector, satisfies the time-independent Schrödinger equation

$$H\psi(\mathbf{r},\mathbf{R})=E\psi(\mathbf{r},\mathbf{R}) , \tag{3}$$

with E the total energy in the center-of-mass system and the Hamiltonian H being given by Eq. (2). Solutions to Eq. (3) must of course obey the usual asymptotic outgoing wave boundary conditions.[30]

In coupled-channel theory, $\psi(\mathbf{r},\mathbf{R})$ is expanded in an orthonormal basis of channel functions $|\varphi_i\rangle$, characterized by the collective quantum number i, resulting in

$$\psi(\mathbf{r},\mathbf{R})=\sum_i \frac{F_i(R)}{R}|\varphi_i\rangle . \tag{4}$$

From Eqs. (3) and (4), by bracketing with $\langle\varphi_i|$, a set of coupled second-order radial differential equations is obtained for the radial wave functions of nuclear motion $F_i(R)$. For the basis set $\{|\varphi_i\rangle\}$ we choose diabatic basis functions that are eigenfunctions of the atomic part $H^{\text{Ne}^{**}}+H^{\text{He}}$ of the Hamiltonian H of Eq. (2).

The coupled equations are then given by

$$\frac{d^2F_i(R)}{dR^2}+\frac{2\mu}{\hbar^2}(E-E^{\text{Ne}^{**}}-E^{\text{He}})F_i(R) = \sum_j \frac{2\mu}{\hbar^2}[\langle\varphi_i|V^{\text{Ne}^{**}\text{-He}}(R)|\varphi_j\rangle + \langle\varphi_i|T_{\text{rot}}|\varphi_j\rangle]F_j(R) . \tag{5}$$

The operator T_{rot} provides rotational coupling; "physical" coupling occurs by the interaction $V^{\text{Ne}^{**}\text{-He}}$. This is in contrast to the adiabatic approach of Hennecart and Masnou-Seeuws, where coupling is caused by the operators T_{rad} and T_{rot}.

The adiabatic and diabatic approaches of course yield equivalent results for equivalent basis sets. Generally speaking, however, where coupling is limited to a few (quasi) molecular states, a fair description is possible with a smaller number of adiabatic states than diabatic states. Where this is not so, no preference exists for either basis in terms of the number of coupled equations to be solved. However, in terms of numerical stability, the adiabatic approach has the disadvantage of involving the calculation of the radial coupling matrix elements by numerical differentiation. This is especially troublesome near so-called avoided crossings of adiabatic potentials. In addition, a diabatic basis set obviates the need for the calculation of adiabatic eigenfunctions.

B. Ω-diabatic basis

We will now discuss our diabatic basis set, as well as its implementation in our coupled-channel code. Asymptotically, an obvious choice of electron basis functions is that of atomic eigenfunctions

$$|\alpha JM_{J_z}\rangle^{\text{Ne}^{**}}|{}^1S_0\rangle^{\text{He}}\equiv|\alpha JM_{J_z}\rangle ,$$

with the magnetic quantum number M_{J_z} taken with respect to the *space-fixed z* axis (i.e., the asymptotic relative velocity). These may be coupled with the space-fixed eigenfunctions $|NM_{N_z}\rangle$ of the rotational energy operator $T_{\text{rot}}=\mathbf{N}^2/2\mu R^2$ to form *N-diabatic* basis functions with total angular momentum quantum number P and well-defined parity $\pi=(-1)^N$,

$$|\varphi_i\rangle^N=|\pi\alpha JNPM_P\rangle .$$

For smaller values of the internuclear distance R, a *body-fixed* coordinate system, with the z' axis along the internuclear axis, is more appropriate ($V^{\text{Ne}^{**}\text{-He}}$ being known in the $|\alpha J\Omega\rangle$ representation). We repeat that the quantum number N is not compatible with $M_{J_{z'}}$, essentially because a rotation of the internuclear axis implies a change of the quantization axis for $M_{J_{z'}}$. We therefore go to a new basis of common eigenfunctions $|PM_PM_{J_{z'}}\rangle$ of the $\mathbf{P}^2$, P_z, and $P_{z'}=J_{z'}$ operators, coupled with atomic eigenfunctions $|\alpha JM_{J_{z'}}\rangle$. This gives basis states $|\alpha JM_{J_{z'}}PM_P\rangle$. To also provide for definitive parity, we subsequently combine opposite $M_{J_{z'}}$ to form *Ω-diabatic* basis functions, where $\Omega\equiv|M_{J_{z'}}|$,

$$|\varphi_i\rangle^\Omega=|\pi\alpha J\Omega PM_P\rangle .$$

Our coupled-channel calculations are performed in the Ω basis. Leaving out the superscript Ω for simplicity, the coupled equations of Eq. (5) are in this representation,

$$\frac{d^2F_i(R)}{dR^2}+\left[k_i^2-\frac{P(P+1)+J(J+1)-2\Omega^2}{R^2}\right]F_i(R) = \sum_j \frac{2\mu}{\hbar^2}\left[\langle\varphi_i|V^{\text{Ne}^{**}\text{-He}}(R)|\varphi_j\rangle - \frac{1}{2\mu R^2}\langle\varphi_i|P_+J_-+P_-J_+|\varphi_j\rangle\right] \times F_j(R) , \tag{6}$$

with $|\varphi_i\rangle\equiv|\pi\alpha J\Omega PM_p\rangle$ the channel functions used, k_i the asymptotic wave number [given by $k_i^2=2\mu/\hbar^2(E-E_i^{\text{Ne}^{**}}-E^{\text{He}})$], and $P_\pm=P_{x'}\pm iP_{y'}$ and $J_\pm=J_{x'}\pm iJ_{y'}$, the body-fixed ladder operators for the total and electronic angular momenta. The differential equations of Eq. (6) are uncoupled with respect to P and parity π. For the ten states $|\alpha_kJ_k\rangle$ of the Ne** multiplet (with $k=1,2,\ldots,10$), it follows directly from $\Omega=0,1,\ldots,J$ that we have 23 basis functions $|\varphi_i\rangle$. In the region where the nondiagonal elements of the physical coupling

matrix become zero, i.e., $V^{Ne^{**}\text{-}He}=0$ for $i\neq j$, it is profitable to switch to the N representation, with basis functions $|\pi\alpha JNPM_P\rangle$, so that the rotational coupling matrix elements also vanish. In this basis the equations of Eq. (5) become completely uncoupled, and we have the usual radial equations for elastic scattering off a spherical long-range potential, namely the diagonal elements of the $V^{Ne^{**}\text{-}He}$ matrix. When these too disappear, the radial equations yield the analytical solutions of spherical Hankel functions of the first and second kind. They make the matching to the asymptotic boundary condition a simple matter.

An interesting aspect of our description of the scattering of Ne** by ground-state He is its analogy to the scattering of particles from an axially symmetric rigid rotor.[31] Coupling of the particle angular momentum with the angular momentum of the rotor to a total angular momentum leads to a coupling of particle and rotor motion, in the same way that the coupling of **J** and **N** to **P** results in the coupling of electron and nuclear motion in the Ne**-He case.

In the actual coupled-channel program, the calculation of S-matrix elements proceeds in several stages. Firstly, for a total number of M channels $|\varphi_j\rangle=|\pi\alpha J\Omega PM_p\rangle$ in the Ω-diabatic representation, we have M linearly independent "mathematical" solution vectors $\mathbf{F}_i(R)$, which vanish at the origin. In practice, these are obtained by starting up $\mathbf{F}_i$ in channel i at a radius R_0, ideally in the classically forbidden region (hard wall at R_0). The coupled differential equations are numerically integrated with a modified Numerov method[32] to a point R_1, where the physical coupling has disappeared: $V_{ij}^{Ne^{**}\text{-}He}=0$ $(i\neq j)$ for $R\geq R_1-\Delta R$. The Ω-diabatic solutions at R_1 and $R_1-\Delta R$ are transformed to the N-diabatic $|\varphi_i\rangle \equiv |\pi\alpha JNPM_p\rangle$ representation. From there on the components of each vector behave independently, as described by the decoupled equations in the N representation. Rather than integrating the latter outward to the asymptotic matching radius R_2, where $V^{Ne^{**}\text{-}He}=0$, we adopt the more stable procedure of integrating inward from R_2, starting with spherical Bessel- and Neumann-like functions. This allows us to express each component of $\mathbf{F}_i$ as a linear combination of basis solutions $I_i(R)$ and $O_i(R)$ with ingoing and outgoing spherical wave behavior at infinity, respectively. The M mathematical solution vectors $\mathbf{F}_i$ are finally combined linearly to construct M "physical" solution vectors $\mathbf{f}_i$ such that

$$(\mathbf{f}_i)_j=I_j(R)-S_{ji}O_j(R)\ . \tag{7}$$

The open-channel matrix of "reflection" coefficients is the desired S matrix.

C. Program performance

In any coupled-channel calculation a choice has to be made concerning starting point, stepsize, and basis set. Bernstein gives an exposé on this subject.[30] As to the starting point, the model potentials of Hennecart and Masnou-Seeuws discussed earlier are given for $R\geq 4.5a_0$ only. The posting of a hard wall at $R=4.5a_0$ is the obvious answer to this problem. This has been done, even though from Fig. 5 it is clear that $R=4.5a_0$ is not yet inside the classically forbidden region. However, for the transitions of interest (mainly those with the $\{\alpha\}_{4,5,6,7}$ group), it has been verified by varying the starting point that the solutions are quite insensitive to this. Calculations with our extended potentials, made for the explicit purpose of evaluating the importance of the inner potential regions, confirm this. As will be seen relevant cross sections differ by at most 25% from the hard-wall results. In this connection, it is worth noting that especially for small R values a problem arises. Without specific precautions, part of the S-matrix elements obtained would be highly unreliable due to the tendency to linear dependence of solution vectors within the numerical noise level which builds up as a function of R. To avoid this we form M new suitable linear combinations of mathematical solution vectors at one or more values of R.[33]

The stepsize, which is of course related to the wavelength λ for the lowest significant $\{\alpha\}_k$ state, was arrived at empirically by evaluating cross-section precision and S-matrix symmetry for a limited number of P values. A stepsize $\Delta R=0.02a_0$ was chosen.

The Ne**-He system comprises $\sum_{i=1}^{10}(J_i+1)=23$ molecular states $|\alpha J\Omega\rangle$. If all ten fine-structure levels in the $Ne^{**}(\{\alpha\}_i;J_i)$ multiplet are included, we have a maximum of 18 coupled equations for each value of total angular momentum P and parity $\pi=\pm 1$. Energy distance to the states of interest being no reliable criterion for the omission of basis states,[30] we have expanded every molecular state $|\alpha J\Omega(R)\rangle$ in its atomic component states $|\alpha J\rangle$. An example of this is given in Fig. 6. The relative unimportance of the $\{\alpha\}_1$ and $\{\alpha\}_3$ components of the $\{\alpha\}_{4,5,6,7}$ molecular states might lead one to drop these from the calculation. Since these are $J=0$ states, only two Ω-diabatic basis states are saved, which is hardly worthwhile.

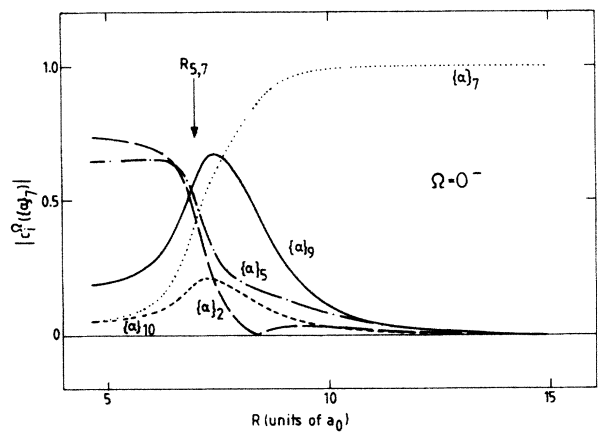

FIG. 6. Coefficients $|C_i^{\Omega}|$ of the $\{\alpha\}_i$ components of the adiabatic Ne**-He eigenstate $|\{\alpha\}_7,\Omega=0^-\rangle$ as a function of the internuclear distance R. The position $R_{5,7}$ of the avoided crossing between the $V_5^{\Omega=0}$ and $V_7^{\Omega=0}$ adiabatic potentials coincides with a significant change in character of the adiabatic eigenstate.

The question of the number of P values to be included in the calculation is more straightforward. We can limit the calculation to those values of P corresponding to impact parameters $b \simeq P\lambda\!\!\!^{-} \leq 15a_0$ (where $V^{Ne^{**}\text{-}He} \simeq 0$), with $\lambda\!\!\!^{-}$ the de Broglie wavelength in the incoming channel. For an energy $E = 100$ meV this amounts to $P \leq 100$. A complete coupled-channel calculation with appropriate integration stepsize $\Delta R = 0.02a_0$ then requires about 2 h on a Burroughs B7900 mainframe computer.

D. Polarized cross sections

Solving the coupled-channel equations yields the S-matrix elements, which in the N representation are defined as

$$S_{lk} \equiv \langle \pi\alpha_l J_l N_l P M_P \mid S \mid \pi\alpha_k J_k N_k P M_P \rangle \ .$$

A representative S-matrix element is displayed in Fig. 7. In general, we have $S(P) = \mid S(P) \mid \exp\{i\varphi[S(P)]\}$. Here the phase $\varphi(S)$ has been plotted as a continuous function of the total angular momentum quantum number P, rather than being limited to $-\pi \leq \varphi(S) \leq +\pi$. We note that "zero points" of the norm $\mid S \mid$ of an S-matrix element correspond to π jumps of the phase $\varphi(S)$. A passage of $S(P)$, between P and $P+1$, almost through the origin of the complex plane into the opposing quadrant implies a phase change $\Delta\varphi(S) = +\pi$ or $-\pi$.

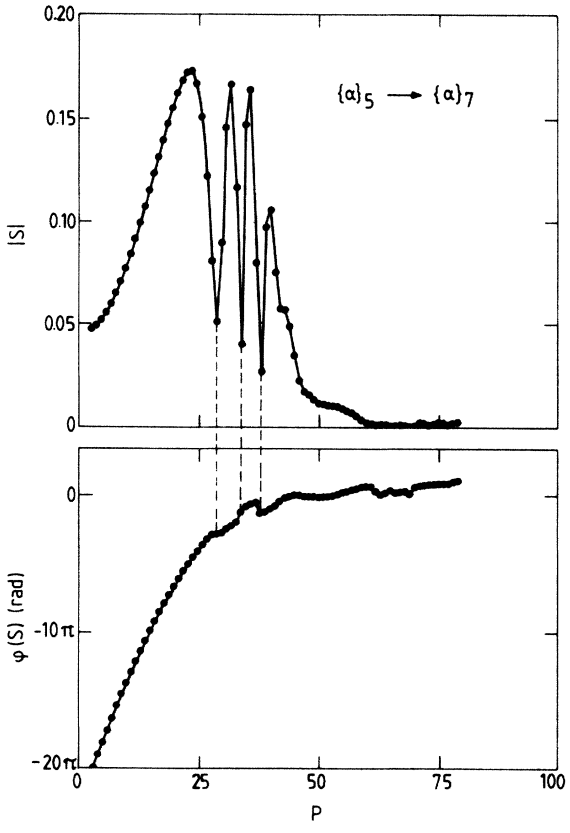

FIG. 7. Absolute value $\mid S(P) \mid$ and phase $\varphi[S(P)]$ of an S-matrix element for the $\{\alpha\}_5 \rightarrow \{\alpha\}_7$ transition over the full range of total angular momentum quantum numbers P [calculation I(a) of Table III]. The phase has been plotted as a continuous function. The dotted lines connect the "zeros" of $\mid S \mid$ with the "π jumps" in $\varphi(S)$.

The single-M_k state polarized cross section $Q_{l\leftarrow k}^{\mid M_k \mid}$ for the $\mid \alpha_k J_k M_{k_z} \rangle \rightarrow \mid \alpha_l J_l \rangle$ transition is given by

$$Q_{l\leftarrow k}^{\mid M_k \mid} = \frac{\pi}{k_k^2} \sum_P (2P+1) q_{l\leftarrow k}^{\mid M_k \mid}(P) \ ,$$

$$q_{l\leftarrow k}^{\mid M_k \mid}(P) = \sum_{N_l} \sum_{N_k} \sum_{N_{k'}} i^{(N_k - N_{k'})} (J_k M_k P - M_P \mid N_k 0) \times (J_k M_k P - M_P \mid N_{k'} 0) \times (S_{lk} - \delta_{\alpha_l \alpha_k} \delta_{N_l N_k}) \times (S_{lk'} - \delta_{\alpha_l \alpha_{k'}} \delta_{N_l N_{k'}})^* \ , \quad (8)$$

with $q_{l\leftarrow k}^{\mid M_k \mid}(P)$ the transition probability for a certain P value. From $\mathbf{P} = \mathbf{J} + \mathbf{N}$, it follows directly that the summation over N values is between $\mid P - J \mid$ and $P + J$. Of course, this is implied by the Clebsch-Gordan coefficients $(J_k M_k P - M_k \mid N_k 0)$ and $(J_k M_k P - M_k \mid N_{k'} 0)$. Also, $M_P \equiv M_k$. Because of the conjugation $*$ in Eq. (8), both phase and absolute value of the complex S-matrix elements are of importance for the polarized cross sections. This is contrary to the unpolarized case, where summation over all orientations $\mid M_k \mid$ of the initial state yields

$$Q_{l\leftarrow k} = \frac{\pi}{k_k^2} \sum_P (2P+1) q_{l\leftarrow k}(P) \ ,$$

$$q_{l\leftarrow k}(P) = \frac{1}{2J_k + 1} \sum_{M_k = -J_k}^{J_k} q_{l\leftarrow k}^{\mid M_k \mid}(P) = \sum_{N_l} \sum_{N_k} (2P+1) \mid S_{lk} - \delta_{\alpha_l \alpha_k} \delta_{N_l N_k} \mid^2 \ . \quad (9)$$

It is for this reason that polarization experiments are ultimately more informative. In Fig. 8 we show the inelastic

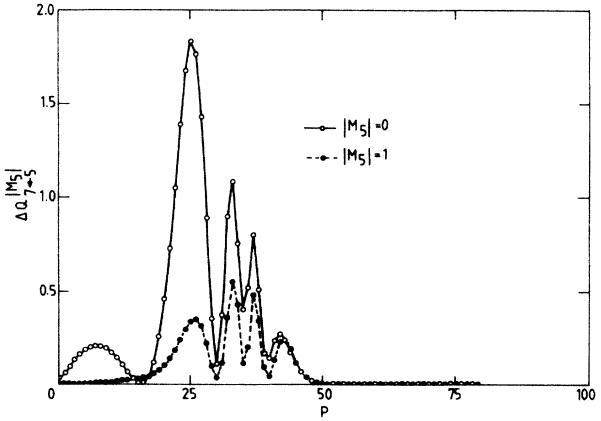

FIG. 8. Contributions $\Delta Q_{7\leftarrow 5}^{\mid M_5 \mid}$ to the pure state polarized cross section $Q_{7\leftarrow 5}^{\mid M_5 \mid}$ for the $\{\alpha\}_5 \rightarrow \{\alpha\}_7$ transition [calculation I(a) of Table III].

TABLE I. Rudimentary comparison between the calculations of the present work and those of Hennecart and Masnou-Seeuws and Hennecart, illustrating the large influence of rotational coupling on cross-section values.

Reference	Input[a]	E_k (meV) $\{\alpha\}_3$	E_k (meV) $\{\alpha\}_4$	$Q_{l\leftarrow k}$ (Å^2) $\{\alpha\}_3\rightarrow\{\alpha\}_4$	$Q_{l\leftarrow k}$ (Å^2) $\{\alpha\}_4\rightarrow\{\alpha\}_5$
Hennecart and Masnou-Seeuws and Hennecart[b]	Two adiabatic states, no rotational coupling	25	32	28	8.7
This work[c]	All states, all couplings	25	32	41	5.3
Hennecart and Masnou-Seeuws and Hennecart[b]	Two adiabatic states, no rotational coupling	25	32	28	8.7
This work	$\{\alpha\}_{3,4,5,6,7}$ only, no rotational coupling	25	32	35	0.5
This work	$\{\alpha\}_{3,4,5,6,7}$ only, all couplings	25	32	51	4.2

[a]All calculations with hard wall at $R=4.5a_0$.
[b]Interpolated values (Refs. 1 and 11).
[c]Calculation II.

$\{\alpha\}_5\rightarrow\{\alpha\}_7$ cross-section contribution per P value, $\Delta Q^{|M_5|}_{7\leftarrow 5}(P)$ for $|M_5|=0$ and $|M_5|=1$. The asymptotic orientation of the Ne** atom is seen to have great influence.

In their two-channel coupled-channel calculations, performed in an adiabatic basis, as opposed to our diabatic basis, Hennecart and Masnou-Seeuws[1] and Hennecart[11] do not take into account the rotational coupling (nor the diagonal $[J(J+1)-\Omega^2]/R^2$ term of the coupling matrix in the Ω-diabatic basis). This prototypical Ω-conserving approach is equivalent to "locking" the electronic angular momentum **J** to the body-fixed internuclear axis. However, we observe a tendency of **J** to remain space fixed down to intermediate R values. Furthermore, of course, in this way it becomes impossible to explain transitions like the $\{\alpha\}_3\rightarrow\{\alpha\}_5$ transition.[11]

In an effort to quantify the differences between the two approaches, we have juxtaposed some results for both types of calculation in Table I. Comparing our calculation at $E_6=100$ meV (all states, all couplings, hard wall) with the calculations of Hennecart and Masnou-Seeuws for the $\{\alpha\}_3\rightarrow\{\alpha\}_4$ and $\{\alpha\}_4\rightarrow\{\alpha\}_5$ transitions at the appropriate energies, we find fair agreement. We note that $Q^{\text{ours}}_{4\leftarrow 3}>Q^{\text{theirs}}_{4\leftarrow 3}$, while for the other transition the situation is reversed: $Q^{\text{ours}}_{5\leftarrow 4}<Q^{\text{theirs}}_{5\leftarrow 4}$. To determine to what extent this must be attributed to the presence or absence of rotational coupling, or to the implicit difference in basis sets, an additional full coupled-channel calculation would be required. We have limited ourselves to less extensive calculations with a basis set consisting of $\{\alpha\}_3$, $\{\alpha\}_4$, $\{\alpha\}_5$, $\{\alpha\}_6$, and $\{\alpha\}_7$ only. With this basis set and leaving out rotational coupling, the results of Hennecart and Masnou-Seeuws for the $\{\alpha\}_3\rightarrow\{\alpha\}_4$ transition are reproduced quite well. This is true over the energy range $0<E<250$ meV. The same cannot be said for the $\{\alpha\}_4\rightarrow\{\alpha\}_5$ transition. Even the much larger cross-section value, obtained with rotational coupling, is somewhat too small. Rotational coupling causes the $\{\alpha\}_3\rightarrow\{\alpha\}_4$ transition to be larger as well, but to a lesser degree. Whereas, of course, the material at hand is too slight to warrant a general conclusion, the above is at least indicative of the importance of rotational coupling. A similar remark can be made concerning the difference in results, obtained from our calculations with full and truncated basis sets.

IV. EXPERIMENTAL SETUP

A. Design

The design of a crossed-beam experiment for the investigation of inelastic collision processes with short-lived, electronically excited atoms has to be considered very carefully. The more so when the reaction products can only be detected through their radiative decay. We assume a configuration of primary beam, secondary beam, and laser beam crossing at right angles. The major experimental problems encountered follow directly from the expressions for the count rates I_k for the direct fluorescence from the initial state $\{\alpha\}_k$, without a secondary beam, and I_l for the collision-induced fluorescence from the final state $\{\alpha\}_l$, respectively. These are given by

$$I_k=\eta_k\dot{N}_k R_k\ , \tag{10a}$$

$$I_l=\eta_l\dot{N}_k R_k\frac{g}{v_1}n_2 l_\tau Q_{l\leftarrow k}\ , \tag{10b}$$

with η_k and η_l the photon detection efficiency for the direct and collision-induced fluorescence, $\dot{N}_k$ (s^{-1}) the flow of initial state particles through the scattering volume, v_1 the primary-beam velocity, g the relative velocity of the collision partners, n_2 the secondary-beam density, $l_\tau=v_1\tau_k=v_1/A_k$ the lifepath of the initial state

particles, and $Q_{l\leftarrow k}$ the total inelastic cross section for the $\{\alpha\}_k \rightarrow \{\alpha\}_l$ transition. Through the factor $R_k \simeq 1/(1-A_{ki}/A_k)$ we take into account that a fraction A_{ki}/A_k of the atoms in the initial short-lived $\{\alpha\}_k$ state is recycled via the metastable Ne*(^3P_J) lower level of the optical pumping transition. With appropriate laser power, almost all of the Ne*(^3P_J) atoms in the primary beam are excited to the $\{\alpha\}_k$ state, resulting in $\dot{N}_k = C_J \dot{N}_{\mathrm{Ne}^*(J)}$, with C_J the relative population of the metastable state used for the Ne**$\{\alpha\}_k$ production. In Eq. (10b) for the collision-induced fluorescence signal we recognize the usual "*nlQ*" product of a crossed-beam experiment, modified by the use of the lifepath l_τ instead of the length of the scattering volume.

From Eq. (10) we can deduce the practical problems which our particular experiment presents. Both the lifepath l_τ of the short-lived atoms and the transition cross section $Q_{l\leftarrow k}$ are very small: $l_\tau \simeq 20$ μm, $Q_{l\leftarrow k} \simeq 1$ Å^2. This means that it takes considerable effort to obtain a measurable collision-induced fluorescence signal, i.e., a signal that can be separated from the inevitable background. Firstly, we must maximize primary-beam flow $\dot{N}_{\mathrm{Ne}^*}$ and secondary-beam density n_2. Secondly, extremely efficient detection of fluorescence photons is needed, that is to say high values of the optical detection efficiency η_l. As to background radiation, from Eqs. (10a) and (10b) it follows that at all times the direct fluorescence radiation $\dot{N}_k$ will be several orders of magnitude larger than the inelastic fluorescence $\dot{N}_l$. This calls for almost complete suppression of $\dot{N}_k$. Of course the same goes for other sources of background radiation.

The above experimental requirements have led us to design a novel crossed-beam apparatus, of which a schematic view is given in Fig. 9. The primary beam of metastable Ne* atoms originates in a discharge excited supersonic expansion, or thermal metastable source[34] (TMS). The differentially pumped source chamber is connected to the main vacuum chamber by a 0.5-mm ϕ skimmer. The maximum centerline Ne*($^3P_2$) intensity for the TMS, operated with pure neon, is about $j_{i,0} \simeq 10^{14}$ s^{-1} sr^{-1}; the $^3P_2$:$^3P_0$ ratio is roughly 5:1. Downstream of the skimmer, all charged particles are removed by condenser plates. A high density of metastable Ne* atoms in the collision region is obtained by virtue of the small distance to the TMS. The collision region being situated about 90 mm downstream of the TMS, we have a primary beam density $n_{\mathrm{Ne}^*} \simeq 10^{13}$ m^{-3}. Metastable particle flow $\dot{N}_{\mathrm{Ne}^*}$ through the collision region is determined by the 1-mm ϕ primary beam defining diaphragm at 60 mm from the skimmer. This geometry results in $\dot{N}_{\mathrm{Ne}^*} \simeq 2\times 10^{10}$ s^{-1}.

The primary beam of metastable Ne* atoms is crossed at right angles by the laser beam from a cw single-mode dye laser system. The laser frequency is stabilized to within 0.5-MHz rms deviation of the transition frequency ν_{ik}.[35] Laser power ($P \leq 0.2$ mW in the collision region) is controlled and stabilized with an electro-optical modulator. The laser beam has a waist in the collision region ($1/e^2$ radius, $W = 0.5$ mm). Because of the short lifetimes of the Ne**$\{\alpha\}_k$ atoms, produced in the optical pumping process, it is the laser beam that determines the lateral position of the collision region. The secondary beam has to pass through the crossing point of the laser and primary beams.

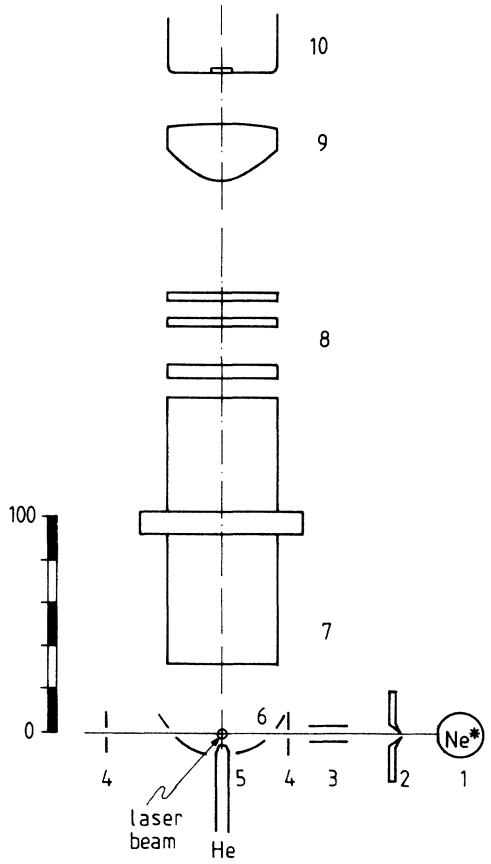

FIG. 9. Schematic view of the experimental setup. The scale is in millimeters. (1) Primary-beam source; (2) skimmer; (3) condenser plates; (4) primary-beam diaphragms; (5) secondary-beam nozzle; (6) parabolic mirror; (7) Plexiglass light guide; (8) interference and cutoff filters; (9) lens; (10) photomultiplier.

A skimmerless supersonic expansion (nozzle diameter $2R_n = 50$ μm) forms the secondary beam. This allows a very small distance from the nozzle to the collision region, and a correspondingly high secondary-beam density. In our apparatus the distance may be adjusted from 0–12 mm, but is typically 2 mm. In that case, for noble-gas atoms, the secondary beam density is given by supersonic expansion theory[36] as $n_2 \simeq 3\times 10^{20}$ m^{-3}. In summary, we have fulfilled the first experimental requirement of high primary- and secondary-beam densities by situating both primary- and secondary-beam sources as close to the collision region as possible.

The demands made of the optical detection system, i.e., a large detection efficiency η and effective suppression of the direct fluorescence radiation, have been met by employing narrow-band interference filters for wavelength selection [2-nm full width at half maximum (FWHM), 10-nm FW at 10^{-6} transmission]. With these we may monitor a single line of either the collision-induced fluorescence from the final state $\{\alpha\}_l$ or the direct

fluorescence from the initial state $\{\alpha\}_k$. More in particular, as the interference filters require perpendicular incidence, the collision region is situated near the focal point of a parabolic mirror. Thus a substantial portion of the fluorescence radiation is imaged into a (nearly) parallel beam. Solid angle efficiency of the parabolic mirror is approximately 0.40, i.e., a solid angle of 1.6π is collected. The condition of (nearly) perpendicular incidence on the interference filters poses no serious limitation to the acceptance of the optical system. The optical phase volume of the parabolic mirror-interference filter combination is very much larger than may be attained with a monochromator. Additional suppression of background light is achieved by the use of colored glass cutoff filters. After passing through the filters, the photons are focused onto the 9-mm ϕ cathode of an S20 photomultiplier in a cooled housing. Quantum efficiency of the photomultiplier is a low 3–5%, depending on the wavelength. When measuring direct fluorescence radiation, grey filters are added to the optical system in order to guarantee a linear response of the photomultiplier. In the present configuration the overall detection efficiency of the optical system is typically $\eta=10^{-3}$ per photon ($\lambda=650$ nm) produced in the collision region. The overall figure of merit in the thermal energy range is about 1 kHz/Å^2, for the number of counts per unit of inelastic total cross section. The background count rate ranges from 2 to 15 kHz and is due mainly to the line emission from the discharge in the TMS.

B. Performance

Of the several noteworthy features of this experiment we here note only 2, both related to the use of a free-jet expansion for our secondary beam. Firstly, before the primary beam ever reaches the scattering center, it is attenuated up to 70% by secondary beam particles, both in the expansion itself and in the form of residual gas. This results in a transmission factor T_k, depending upon the position x along the primary-beam axis, that is given by

$$T_k(x)=\dot{N}_k(x)/\dot{N}_k(-\infty) = \exp\left[-\int_{-\infty}^{x}\frac{g(x')}{v_1}n_2(x')Q\,dx'\right]. \quad (11)$$

Here Q is the effective total cross section for elastic scattering of Ne* atoms by He atoms. Of course, this factor enters into both signals I_l and I_k for collision-induced and direct fluorescence, respectively. For the ratio of these two signals we have, in more specific terms than offered by Eq. (10),

$$\frac{I_l}{I_k}=\frac{\int_V \eta_l(\mathbf{r})n_k(\mathbf{r})n_2(\mathbf{r})g(\mathbf{r})Q_{l\leftarrow k}(g)d\mathbf{r}}{A_k\int_V \eta_k(\mathbf{r})n_k(\mathbf{r})d\mathbf{r}}, \quad (12)$$

the integral being taken over the scattering volume V. To first order, and in keeping with Eq. (10), this reduces to

$$\frac{I_l}{I_k}\simeq\frac{\eta_l}{\eta_k}\frac{g}{v_1}n_2 l_\tau Q_{l\leftarrow k}. \quad (13)$$

The small size of the scattering region, as determined by the density profile $n_k(\mathbf{r})$ of the short-lived $\{\alpha\}_k$ atoms, ensures that Eq. (13) is indeed a fair approximation of Eq. (12).

Since we are concerned only with the ratio I_l/I_k, neither the potentially troublesome attenuation phenomenon nor a number of other unknown *common* factors preclude the possibility of obtaining absolute cross section values. This is illustrated by Figs. 10 and 11. Figure 10 shows T_k, measured by looking at the direct fluorescence signal I_k as a function of secondary-beam reservoir pressure p_{He}. Agreement with Eq. (11) is very good. By inserting into Eq. (11) the secondary-beam density profile, we find from these and other measurements that $Q\simeq 100$ Å^2, which is a reasonable value for hard-sphere scattering. In Fig. 11 we have plotted the ratio I_l/I_k of collision-induced and direct fluorescence signals as a function of the pressure p_{He}. The linear dependence of $I_l/I_k\sim n_2 l_\tau Q_{l\leftarrow k}$ on p_{He}, in contrast to the behavior of T_k, provides convincing evidence of the soundness of the principles embodied in our experiment.

As a second characteristic of our present setup, the scattering center position is ultimately determined by laser beam alignment. Since secondary-beam density, among others, does not factor out from the ratio of fluorescence signals, this alignment takes on a critical importance, as evidenced by Fig. 12 of the ratio I_l/I_k versus laser beam position along the primary-beam axis.

Given the position of the scattering center, either Eq. (12) or Eq. (13) can be used to obtain absolute cross-section values. Of the quantities in these equations, the secondary-beam density n_2 is directly related to the

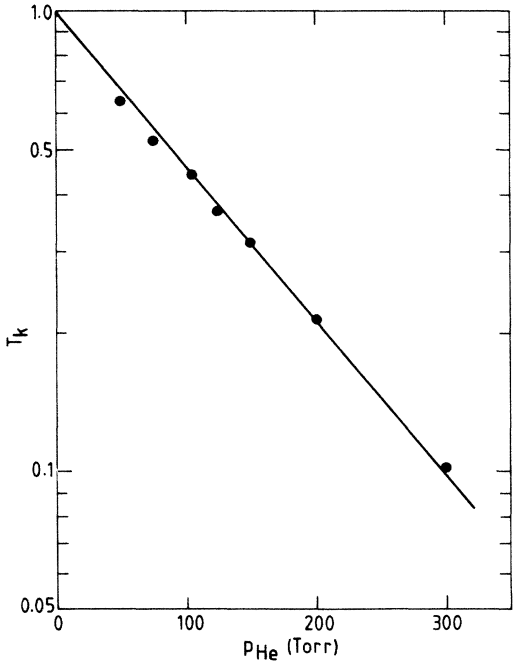

FIG. 10. Primary-beam transmission factor T_k as a function of secondary-beam reservoir pressure p_{He}. The observed exponential attenuation conforms with Eq. (11), with a cross section $Q\simeq 100$ Å^2 for Ne*($^3P_0$)-He collisions.

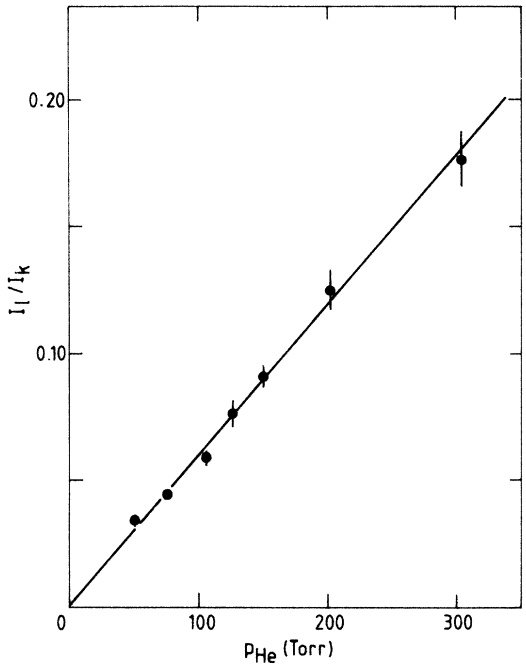

FIG. 11. Collision-induced to direct fluorescence ratio I_l/I_k as a function of secondary-beam reservoir pressure p_{He}. As expected from Eq. (12), the ratio I_l/I_k does not depend on the primary-beam transmission factor T_k, but is proportional to $n_2 \sim p_{He}$.

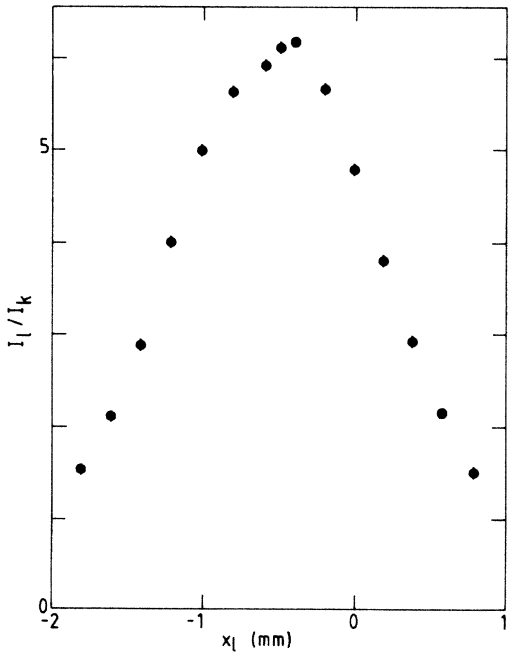

FIG. 12. Collision-induced to direct fluorescence ratio I_l/I_k as a function of laser beam position x_l along the primary-beam axis. The result reflects mainly the secondary-beam density profile.

source density n_{He} through the shape of the radially expanding flow field. For monoatomic gases, with the nozzle shape used in our setup, experiments and theory are in good agreement.[36] The position dependence of the detection efficiency η was calculated, following a separate calibration of the optical system's various components. To our advantage, only the ratio η_l/η_k is of importance. Under the simplifying assumption of monoenergetic particle beams, the position dependence of the relative velocity g is purely a matter of geometry. For use in Eq. (13), model calculations for the optical pumping process yield the distribution n_k of the short-lived atoms over the scattering volume. We find that cross sections, calculated with Eq. (13), differ by typically 20% from those following from Eq. (12).

C. Measuring routine

Our aim is to determine the collision-induced and direct fluorescence signals I_l and I_k, as defined in Eq. (12). Ideally, this would involve two measurements only, with different optics (interference filters). In practice, however, we will have to correct for background light which cannot be entirely suppressed by the optical system.

In order to correct for background contributions, two further diagnostics are employed in addition to the use of different *filters* for direct and collision-induced fluorescence. The first of these is modulation of the optical pumping process by which the initial $Ne^{**}\{\alpha\}_k$ atoms are produced. Rather than simply turning the laser "on" and "off", which allows for no easy correction for stray laser light, the *laser* is tuned and detuned sufficiently (about 100 MHz) to preclude excitation of the metastable $Ne^*(^3P_J)$ atoms. The slight accompanying wavelength change makes no difference to the optical system. The second additional diagnostic is modulation of the *secondary beam,* by simply turning it on and off. Of course, this also influences the attenuation of the primary beam by secondary-beam particles. By combining these three modulation techniques, which are all under computer control, we can easily design a strategy to eliminate all background contributions.

A paper, offering a more detailed description of the design of the apparatus and the execution of the measurements, is forthcoming.[37]

V. EXPERIMENTAL RESULTS FOR POLARIZED CROSS SECTIONS

In our experiment, the short-lived $Ne^{**}\{\alpha\}_k$ atoms are prepared in a polarized state, consisting of an incoherent distribution over substates $|\alpha_k J_k m_k\rangle$ with respect to the excitation process quantization axis. The associated probabilities are g_{m_k}. As a linearly polarized laser is used to excite the metastable Ne^* atoms, the natural excitation axis for the optical pumping process is along the laser electric field **E**. The quantization axis for the collision process is the asymptotic relative velocity **g** of the collision partners. For a given angle β between **E** and **g**, and suitable orientations of the remaining axes perpendicular

to the quantization axis, the initial state $|\alpha_k J_k m_k\rangle_{\mathcal{E}}$ can be written as

$$|\alpha_k J_k m_k\rangle_{\mathbf{E}} = \sum_{M_k} d^{J_k}_{m_k M_k}(\beta)\,|\alpha_k J_k M_k\rangle_{\mathbf{g}}\ , \tag{14}$$

with d the usual rotation matrices or reduced Wigner D functions.[38] The observed total cross section $Q^{\beta}_{l\leftarrow k}$ is now found to be an incoherent sum over the single M_k-state polarized cross sections $Q^{|M_k|}_{l\leftarrow k}$ of Eq. (7),

$$Q^{\beta}_{l\leftarrow k} = \sum_{m_k} g_{m_k} \sum_{M_k} (d^{J_k}_{m_k M_k}(\beta))^2 Q^{|M_k|}_{l\leftarrow k}\ . \tag{15}$$

This incoherence with respect to M_k is essentially due to the fact that the final atomic polarization and direction of motion are not observed. The unpolarized cross section

$$Q_{l\leftarrow k} = \frac{1}{2J_k+1} \sum_{M_k} Q^{|M_k|}_{l\leftarrow k} \tag{16}$$

is of course independent of the quantization axis.

A. The ($\{\alpha\}_5, J_5=1$) initial state

We will first discuss a number of transitions which have in common the $\{\alpha\}_5$ initial state, as produced from the Ne*($^3P_0$) metastable state. For this $J_5=1$ state, distribution over the magnetic substates will be according to

$$g_{m_k=0} = 1\ , \tag{17a}$$

$$g_{|m_k|=1} = 0\ . \tag{17b}$$

The cross section $Q^{\beta}_{l\leftarrow k}$ of Eq. (15) now becomes

$$Q^{\beta}_{l\leftarrow k} = \tfrac{1}{2}(Q^{|0|}_{l\leftarrow k} + Q^{|1|}_{l\leftarrow k}) + \tfrac{1}{2}(Q^{|0|}_{l\leftarrow k} - Q^{|1|}_{l\leftarrow k})\cos(2\beta)\ , \tag{18}$$

where ultimately the polarized cross sections $Q^{|M_k|}_{l\leftarrow k}$ are of interest. As may be seen from Eq. (18) for $J_k=1$, measurement of $Q^{\beta=0}_{l\leftarrow k}$ and $Q^{\beta=\pi/2}_{l\leftarrow k}$ suffices to determine $Q^{|0|}_{l\leftarrow k}$ and $Q^{|1|}_{l\leftarrow k}$. Both from the standpoint of detecting unforeseen physical effects and for the additional check it provides in the crucial matter of laser beam alignment, the coverage of a more extensive range of β values is desirable.

In Fig. 13 we show the diagram of velocity vectors in the laboratory system. The relation between β and the laser polarization angle θ_E depends on the scattering center position x_s, relative to the centerline of the secondary beam. Equation (18) can help us calibrate the zero of the x scale. For a given position, the extrema of $Q_{l\leftarrow k}$ as a function of ϑ_E correspond to $\beta=0$ and $\pi/2$, with only the identification of the extremum belonging to $\beta=0$ left open. This problem can be solved unequivocally by measuring $Q_{l\leftarrow k}$ for some different positions x_s and primary-beam velocities $\mathbf{v}_1$. Once this calibration has been performed the x scale is permanently coupled to the scale of the laser beam translator.[39]

The experiments under discussion have been performed by pumping the $\{\alpha\}_5$ level through the Ne*($^3P_0$)$\rightarrow\{\alpha\}_5$ transition at $\lambda=626.6$ nm. The $\{\alpha\}_4$, $\{\alpha\}_6$, and $\{\alpha\}_7$ states have been detected by observing the radiative decay at $\lambda=667.8$, 693.2, and 653.3 nm, respectively. In Figs. 14, 15, and 16 we show the experimental results $Q^{\beta}_{l\leftarrow k}$ for the $\{\alpha\}_5\rightarrow\{\alpha\}_4$, $\{\alpha\}_6$, and $\{\alpha\}_7$ transitions, obtained by scanning the angle θ_E over the full range $-105°\le\theta_E\le 105°$.

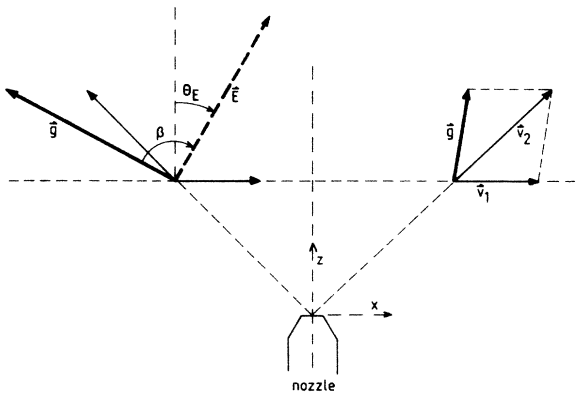

FIG. 13. Newton diagram of the collision process, with $\mathbf{v}_1$ and $\mathbf{v}_2$ the primary- and secondary-beam velocities. Upstream of the secondary-beam nozzle, the relative velocity g is high; downstream, it is low. The angle β between the relative velocity $\mathbf{g}$ and the laser electric field vector $\mathbf{E}$ has been indicated.

Among the pictured transitions with $\{\alpha\}_5$ as an initial state, the whole gamut of possible polarization effects is

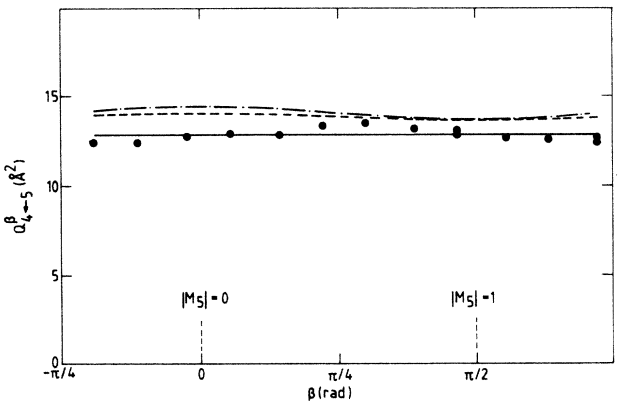

FIG. 14. Experimental results for the observed cross section $Q^{\beta}_{4\leftarrow 5}$ as a function of the angle β between the electric field $\mathbf{E}$ of the laser and the relative velocity $\mathbf{g}$ at a center-of-mass energy $E_5=100$ meV. The statistical errors are smaller than the size of the data points. The observed dependence on β reflects the nonisotropic distribution of collision-induced fluorescence radiation. The solid line (——) therefore indicates the average value of the data points and does not represent a curve fit according to Eq. (18). The other lines are the results of calculations with the model potentials of Hennecart and Masnou-Seeuws (— — —) and the extended potentials (—·—·—·) of Sec. II B as input.

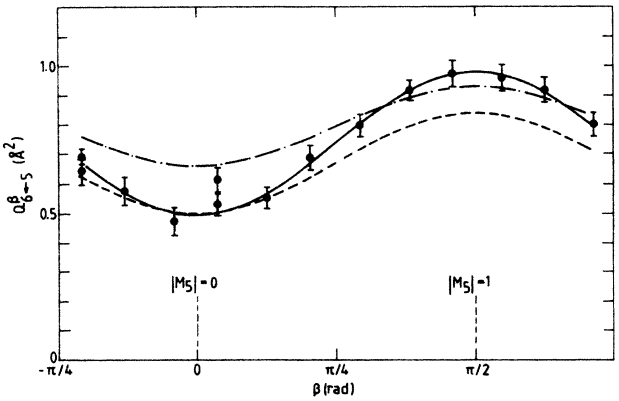

FIG. 15. Experimental results for the observed cross section $Q^{\beta}_{6\leftarrow5}$ as a function of the angle β between the electric field **E** of the laser and the relative velocity **g** at a center-of-mass energy $E_5=100$ meV. Statistical errors only have been indicated. The solid line (——) represents a curve fit of the data points according to Eq. (18). The other lines are the results of calculations with the model potentials of Hennecart and Masnou-Seeuws (— — —) and the extended potentials of Sec. II B (—·—·—·) as input.

observed. At the present energy we find that $Q^{|0|}_{4\leftarrow5}\simeq Q^{|1|}_{4\leftarrow5}$, $Q^{|0|}_{6\leftarrow5}<Q^{|1|}_{6\leftarrow5}$, and $Q^{|0|}_{7\leftarrow5}>Q^{|1|}_{7\leftarrow5}$. The polarization effect in the $\{\alpha\}_5\rightarrow\{\alpha\}_7$ transition is particularly pronounced. The $Q^{\beta}_{6\leftarrow5}$ and $Q^{\beta}_{7\leftarrow5}$ clearly conform to the cos2β expression of Eq. (18). The somewhat deviating behavior of the $Q^{\beta}_{4\leftarrow5}$ cross section appears to be caused by the nonisotropic distribution of collision-induced fluorescence radiation, for which at present we do not correct and which takes on importance in the absence of a real polarization effect. The shifted extrema, at approximately $\theta_E=0$ and $\pi/2$, are traceable to the symmetry axis of the apparatus at $\theta=0$ and not to the initial J_k orientation. As to the cross-section magnitude, the variation there is considerable as well, with $Q_{4\leftarrow5}$ and $Q_{6\leftarrow5}$ at opposite ends of the scale. The resulting experimental polarized cross sections $Q^{|M_k|}_{l\leftarrow k}$, derived from a least-squares fit of the data points to Eq. (18), have been summarized in Table II.

With our coupled-channel code, we have computed polarized cross sections $Q^{|M_k|}_{l\leftarrow k}$ at energies $E_5=100$ meV [calculation I(a)] and $E_6=100$ meV [(calculation I(b)], relative to the indicated initial state. The model potentials of Hennecart and Masnou-Seeuws[1] and Hennecart[11] were used. Of necessity, a hard wall at $R=4.5a_0$ was introduced. In additional calculations at $E_5=100$ meV [II(a)] and $E_6=100$ meV [II(b)], the extended potentials of Fig. 4 were used. The characteristics of the coupled-channel calculations have been summarized in Table III. The results of these calculations are given in Figs. 14–16, as well as in Table II.

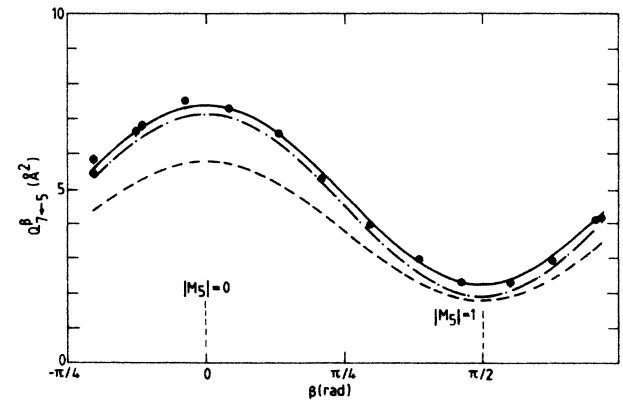

FIG. 16. Experimental results for the observed cross section $Q^{\beta}_{7\leftarrow5}$. See caption of Fig. 15 for further detail.

TABLE II. Observed and calculated polarized cross sections $Q^{|M_k|}_{l\leftarrow k}$ at center-of-mass energy $E=100$ meV. The potentials used in the calculations [I(a), I(b), II(a), and II(b)] are described in Table III.

		$Q^{\|M_k\|}_{l\leftarrow k}$ (Å^2)		
			Calculated	
$\{\alpha\}_k\rightarrow\{\alpha\}_l$	$\|M_k\|$	Experimental	[I(a), I(b)]	[II(a), II(b)]
$\{\alpha\}_5\rightarrow\{\alpha\}_4$	0	13.2	14.0	14.4
	1	12.5	13.7	13.7
$\{\alpha\}_5\rightarrow\{\alpha\}_6$	0	0.50	0.50	0.66
	1	0.97	0.84	0.93
$\{\alpha\}_5\rightarrow\{\alpha\}_7$	0	7.0	5.8	7.1
	1	2.0	1.8	1.9
$\{\alpha\}_6\rightarrow\{\alpha\}_7$	0	8.3	7.3	7.8
	1	6.3	7.1	6.0
	2	3.1	3.0	3.1

As far as the $\{\alpha\}_5\rightarrow\{\alpha\}_l$ transitions are concerned, there is excellent agreement between theory and experiment: not only the polarization effects $Q^{|0|}_{l\leftarrow k}/Q^{|1|}_{l\leftarrow k}$, but even the absolute cross-section values are reproduced well. Cross sections from the preliminary calculation with model potentials extended down to $R=2a_0$ differ from the hard-wall results by 30% at most, which is of the order of the experimental errors. We have thus explicitly verified the relative unimportance of the inner region ($R\leq4.5a_0$) of the Ne**-He potentials for the above transitions and energies.

To obtain a qualitative insight into the mechanisms underlying the surprisingly large polarization effects, we have to consider the salient features of the adiabatic potential curves involved, as calculated by Hennecart and Masnou-Seeuws[1] and Hennecart[11] with a model potential method. Indeed, the choice of the $\{\alpha\}_{4,5,6,7}$ states as objects of our primary interest was dictated by the presence of several clear-cut avoided crossings between their adiabatic potentials.

We first discuss the $\{\alpha\}_5\rightarrow\{\alpha\}_7$ transition of Fig. 16.

TABLE III. Characteristics of the coupled-channel calculations, performed in this work.

Calculation	Energy (meV)	Potentials
I(a)	$E_5=100$	Hard wall
I(b)	$E_6=100$	Hard wall
II(a)	$E_5=100$	Extended
II(b)	$E_6=100$	Extended

Both the $\{\alpha\}_5$ and $\{\alpha\}_7$ states, but the former in particular, show only a small splitting between the $\Omega=0$ and 1 molecular potentials. To indicate the probed range of internuclear distances R: at $E=100$ meV the classical turning point for both Ω potentials of the $\{\alpha\}_5$ state is $R_t=6a_0$ for an impact parameter $b=0$ and $R_t=7.1a_0$ for $b=6a_0$. For $\Omega=0$ the adiabatic electronic states are divided into 0^+ and 0^- classes, depending on the reflection symmetry. The $\Omega=0^-$ class contains the $\{\alpha\}_{2,5,7,9,10}$ odd-J states and there is a strong coupling of the $\{\alpha\}_5$ and $\{\alpha\}_7$ states. This coupling can be identified as an avoided crossing at $R_c=7.0a_0$, with a Landau-Zener-type coupling matrix element $H_{57}=22$ meV (half the smallest separation of the potential curve), which is very large in comparison with the energy difference $\Delta E_{57}=80.7$ meV of the $\{\alpha\}_5$ and $\{\alpha\}_7$ states at infinity. For $\Omega=1$ there is no symmetry constraint and the intermediate $\{\alpha\}_6$ state disturbs the coupling of the $\{\alpha\}_5$ to the $\{\alpha\}_7$ state. We now observe an avoided crossing of the $\{\alpha\}_6$ and $\{\alpha\}_7$ states at $R_c=7.5a_0$ with $H_{67}=3.5$ meV. Moreover, the initial $\{\alpha\}_5$ state is now coupled to the $\{\alpha\}_4$ state by an avoided crossing with $H_{45}=1.0$ meV at $R_c=8.5a_0$. The contribution of the $\Omega=1$ orientation to the $\{\alpha\}_5\rightarrow\{\alpha\}_7$ transition is small due to the strong coupling of both the initial and final state to the $\{\alpha\}_4$ and $\{\alpha\}_6$ states, respectively, which is absent for the $\Omega=0^-$adiabatic potentials. The large coupling matrix element H_{57} for $\Omega=0^-$ is consistent with a main contribution to the cross section from small impact parameters, where radial velocities are large. Even without "locking" of the initial $\Omega=|M_J|$ orientation to the internuclear axis this orientation will then be largely conserved at the crossing radius. This explains the large polarization effect $Q_{7\leftarrow5}^{|0|}\gg Q_{7\leftarrow5}^{|1|}$.

The picture that thus emerges is confirmed by the $\{\alpha\}_5\rightarrow\{\alpha\}_4$ transition, for which the results are shown in Fig. 14. We note the absence of a significant polarization effect. This is in apparent contradiction with the simultaneous presence of an avoided crossing of the $\{\alpha\}_5$ and $\{\alpha\}_4$ states for the $\Omega=1$ orientation, and the absence of any coupling at all for $\Omega=0$, where initial and final states are in different symmetry classes. However, because of the small splitting of the $\Omega=0$ and 1 adiabatic potentials for the $\{\alpha\}_5$ state, the locking of the initial orientation to the internuclear axis constitutes only a minor effect. The asymptotic $|M_J|=0$ orientation will thus be partially rotated at the crossing radius into a local $\Omega=1$ state, which does couple with the final $\{\alpha\}_4$ state. This effect will be most pronounced for large impact parameters. Because of the very small coupling matrix element H_{45}, which requires small values of the radial velocity for optimum coupling, we indeed expect a predominant contribution from large impact parameters. Hence the absence of a polarization effect, $Q_{4\leftarrow5}^{|0|}\approx Q_{4\leftarrow5}^{|1|}$, is qualitatively understood. A similar reasoning may be applied to the other transitions within the $\{\alpha\}_{4,5,6,7}$ group.

B. The ($\{\alpha\}_6, J_6=2$) initial state

As opposed to the $\{\alpha\}_5$ state where $J_5=1$, the $\{\alpha\}_6$ state has $J_6=2$, and must be excited from the Ne*($^3P_2$) state. From the metastable Ne*($^3P_2$) state we may in principle excite states $\{\alpha\}_k$ with either $J_k=1$, 2, or 3. For $J_k=1$, however, an isotropic distribution over m_k substates will result. For $J_k=2$, in the assumed absence of a magnetic field, we find

$$g_{m_k=0}=0\ , \tag{19a}$$

$$g_{|m_k|=1}\simeq\tfrac{1}{6}\ , \tag{19b}$$

$$g_{|m_k|=2}\simeq\tfrac{2}{6}\ , \tag{19c}$$

for the (time-integrated) distribution over magnetic substates in the scattering volume, to be substituted in the general formula

$$\begin{aligned}Q_{l\leftarrow k}^{\beta}=\tfrac{1}{64}\{&[(22g_0+24g_1+18g_2)Q_{l\leftarrow k}^{|0|}+(24g_0+64g_1+40g_2)Q_{l\leftarrow k}^{|1|}+(18g_0+40g_1+70g_2)Q_{l\leftarrow k}^{|2|}]\\&+[(24g_0-24g_2)Q_{l\leftarrow k}^{|0|}+(32g_1-32g_2)Q_{l\leftarrow k}^{|1|}+(-24g_0-32g_1+56g_2)Q_{l\leftarrow k}^{|2|}]\cos2\beta\\&+[(18g_0-24g_1+6g_2)Q_{l\leftarrow k}^{|0|}+(-24g_0+32g_1-8g_2)Q_{l\leftarrow k}^{|1|}+(6g_0-8g_1+2g_2)Q_{l\leftarrow k}^{|2|}]\cos4\beta\}\ .\end{aligned} \tag{20}$$

The experimental results for the $\{\alpha\}_6\rightarrow\{\alpha\}_7$ transition are displayed in Fig. 17. The $\{\alpha\}_6$ state was excited from the Ne*($^3P_2$) state at $\lambda=614.3$ nm. Detection took place at $\lambda=692.3$ and 653.3 nm for the $\{\alpha\}_6$ and $\{\alpha\}_7$ states, respectively. The center-of-mass energy was approximately $E_6=95$ meV, rather than 100 meV as in the $\{\alpha\}_5$ measurements, due to a small difference in laser beam alignment. We observe that in $Q_{7\leftarrow6}^{\beta}$ the presence of the higher-order cos4β term of Eq. (20) is not immediately apparent. The experimental polarized cross sections $Q_{7\leftarrow6}^{|M_6|}$, derived using Eqs. (19) and (20), are given in Table II.

Comparison with the results of the coupled-channel calculations, also given in Table II, again shows excellent agreement. This is true both for the calculation using the hard wall potentials [I(b)] and for that using the extended potentials [II(b)], but for the latter in particular. Strictly speaking, of course, for a more balanced judgment a detailed examination of the distribution parameters g_{m_k} of Eq. (19) is needed. Developments which will enable us to perform this kind of calculation, taking into account the presence of small magnetic fields, are under way.

For a better understanding of the relatively small polarization effect $Q_{7\leftarrow6}^{|0|}/Q_{7\leftarrow6}^{|1|}$, it is sufficient to point to the similarity of the avoided crossing for the $\{\alpha\}_6$ and $\{\alpha\}_7$ states for $\Omega=1$ to that for the $\{\alpha\}_4$ and $\{\alpha\}_5$ states.

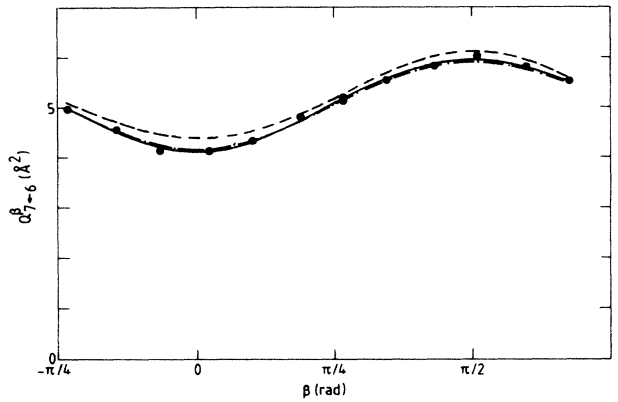

FIG. 17. Experimental results for the observed cross section $Q^{\beta}_{7\leftarrow 6}$. Curve fit of data points (——) according to Eq. (19). See caption of Fig. 15 for further detail.

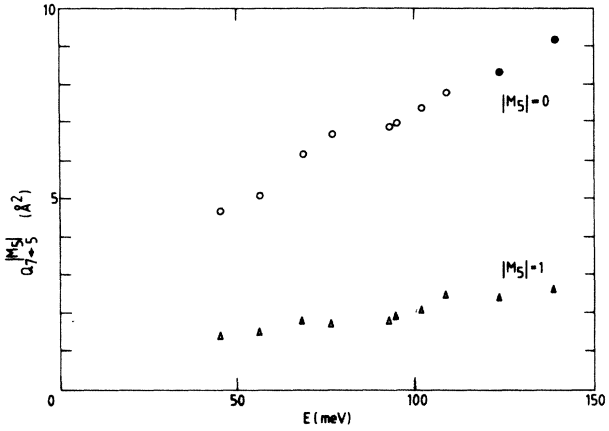

FIG. 19. Energy dependence of the polarized cross sections $Q^{|0|}_{7\leftarrow 5}$ and $Q^{|1|}_{7\leftarrow 5}$. See caption of Fig. 18 for further detail.

Once again, a grazing impact is favored, at slightly higher radial velocities. The smaller crossing radius is bound to lead to smaller cross sections than for the $\{\alpha\}_5 \rightarrow \{\alpha\}_4$ transition, though in itself not by the amount evidenced by the experimental cross sections.

VI. ENERGY DEPENDENCE AND ABSOLUTE VALUES

A. Energy dependence

We have performed measurements of the energy dependence of the $Q^{|M_5|}_{7\leftarrow 5}$ and $Q^{|M_5|}_{4\leftarrow 5}$ cross sections for Ne**-He. This has been done, both by varying the magnitude of the primary-beam velocity v_1 (by using a 85% He-15% Ne seeded primary beam) and by varying the direction of v_2 (by scanning the laser beam along the primary-beam axis). While primary-beam velocities have been determined through time-of-flight measurements, employing a pseudorandom optical chopper,[37] at this stage no attempt has been made to resolve collision-induced fluorescence spectra. Here, as elsewhere, velocity-averaged results only are presented, both as to measured (Ne*) and as to calculated (He) velocity distributions.

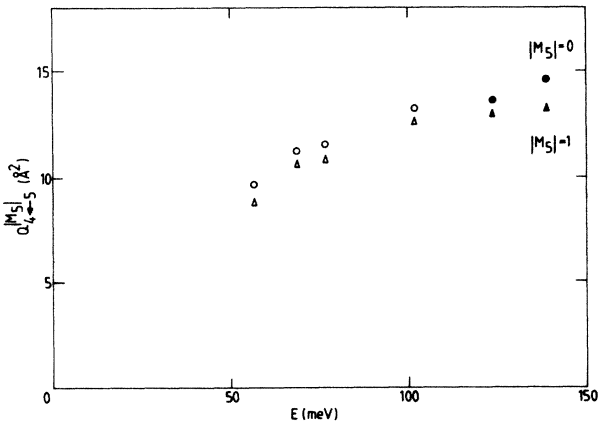

FIG. 18. Energy dependence of the polarized cross sections $Q^{|0|}_{4\leftarrow 5}$ and $Q^{|1|}_{4\leftarrow 5}$, with E the center-of-mass energy. The full points have been obtained by varying the magnitude of the primary-beam velocity v_1; the open points by varying the position of the laser beam along the primary-beam axis, resulting in a different direction of v_2.

The observed energy dependence of the polarized atom cross sections $Q^{|M_5|}_{4\leftarrow 5}$ and $Q^{|M_5|}_{7\leftarrow 5}$ is shown in Figs. 18 and 19. The data points at approximately 60 meV represent the low-end limit of the position-dependent energy variation with the He secondary beam. Likewise, 150 meV is the maximum attainable practical energy with the above seeded primary beam. Errors in the average energy are typically 5%, due to uncertainties in the present laser beam alignment technique.

A detailed discussion of these results on the basis of quantum-mechanical coupled-channel calculations would require a prohibitively large amount of computer time. An analysis in semiclassical terms[40] is less demanding in this respect and seems highly appropriate in view of the pronounced avoided crossings between the adiabatic potentials of Fig. 5.

B. Various other transitions

In addition to the polarization measurements reported above we have performed a number of exploratory measurements under much less well-defined experimental conditions. Their purpose was to establish the presence or absence, within experimental limits, of various transitions. The range of these measurements was determined by filter availability and dye laser operation. Only order-of-magnitude results at an approximate energy $E = 100$ meV are presented in Table IV. The substantial $\{\alpha\}_5 \rightarrow \{\alpha\}_{10}$ transition probability is at first sight rather surprising given the large energy distance $\Delta E_{5,10} = 312$ meV. When using the two-level system $\{\alpha\}_9$ state as an initial state, experimental signals are especially large, due to the replacement of the lifepath l_τ by the laser beam width in Eq. (10), allowing detection of smaller cross sec-

TABLE IV. Order of magnitude of some observed cross sections $Q_{l\leftarrow k}$ at approximate center-of-mass energy $E = 100$ meV. In case of a fluorescence signal below the experimental threshold, an upper limit for the relevant cross section is given. Also shown are calculated unpolarized cross sections. Only for the $\{\alpha\}_5$ [calculations I(a), II(a)] and $\{\alpha\}_6$ [calculations I(b),II(b)] initial states, the collision energy E conforms to the experiment. In some other cases the results of the calculation providing the closest energy match are given between parentheses.

			$Q_{l\leftarrow k}$ (Å^2)					
	Initial state k		Final state l					
k		E_k (meV)	4	5	6	7	8	10
2	Expt.	100			<0.1	<0.1	<0.1	
	Calc.	(67[a]/67[b])			(0.04/0.06)	(0.2/0.2)	(0.0/0.1)	
5	Expt.	100	12.7		0.8	3.7	0.6	0.3
	Calc.	100[a]/100[b]	13.8/13.9		0.8/0.8	3.1/3.6	0.4/1.1	0.0/0.05
6	Expt.	100	0.4	0.4		4.7		<0.1
	Calc.	100[c]/100[d]	0.1/0.2	0.03/0.3		5.5/5.2		0.0/0.04
7	Expt.	100	0.4	0.3	3.2		9.0	
	Calc.	124[c]/(181[b])	0.6/(2.2)	0.7/(2.0)	7.4/(8.7)		8.2/(10.8)	
8	Expt.	100			0.1	<0.1		1.9
	Calc.							
9	Expt.	100			0.01	0.1		2.5
	Calc.							

[a]Calculation I(a).
[b]Calculation II(a).
[c]Calculation I(b).
[d]Calculation II(b).

tions. The $\{\alpha\}_9 \rightarrow \{\alpha\}_6$ transition is an example of this.

When comparing, in Table IV, experimental cross sections with unpolarized quantum-mechanical cross sections $Q_{l\leftarrow k}$ from calculations I(a), I(b), II(a), and II(b), allowances must of course be made for the imperfect energy match of other than the $\{\alpha\}_5 \rightarrow \{\alpha\}_l$ and $\{\alpha\}_6 \rightarrow \{\alpha\}_l$ transitions. The relevant energies have been indicated in the table. On account of the energy mismatch we have refrained from giving the calculated $Q_{l\leftarrow 8}$ and $Q_{l\leftarrow 9}$ cross-section values. Preliminary calculations seem to indicate an inability of coupled-channel calculations with the model potentials of Hennecart and Masnou-Seeuws to predict the considerable $Q_{10\leftarrow 8}$ and $Q_{10\leftarrow 9}$ cross sections, while our extended potentials fare somewhat better in this respect. Apart from that there is rough qualitative agreement between theory and experiment considering the experimental and computational limitations of the comparison. A similar remark can be made with respect to rate constants available from the literature. Again, a proper comparison awaits semiclassical calculations on the energy dependence of cross sections.[40]

Statistical errors in the experimental data are, on the whole, small for all but the weak transitions. In view of the inherent experimental difficulties, discussed earlier, this speaks well for the design of the apparatus. The overall systematic error of our absolute cross-section values we currently estimate at a respectable 30%, laser beam alignment being the main limiting factor. We are working on an automated alignment procedure that will constitute a definite improvement in this regard.[37]

The absolute cross-section values given here for the $\{\alpha\}_5 \rightarrow \{\alpha\}_7$ and $\{\alpha\}_5 \rightarrow \{\alpha\}_4$ transitions differ somewhat from those cited in an earlier paper.[19] This is due almost exclusively to a more recent set of lifetime values[41] having been used in their calculation, different from that used earlier.[42]

VII. CONCLUDING REMARKS

At the investigated thermal energies, where mainly the long-range interactions are probed, quantum-mechanical coupled-channel calculations on the basis of the model potentials of Hennecart and Masnou-Seeuws appear to offer a very satisfactory description of our Ne**-He experimental results. In particular, this is true for the transitions within the $\{\alpha\}_{4,5,6,7}$ group of states. For other transitions, which so far have been explored much less intensively, the general trend is reproduced as well. There are indications that for some of these transitions the inner potential regions, which are not covered by the model potential method, are of importance.

It is possible to obtain a qualitative insight into the mechanisms underlying the coupled-channel and experimental results by considering the adiabatic potentials calculated from the model potentials. Our present understanding is based on the constraints of symmetry, the occurrence of avoided crossings between the potential curves, and the partial absence of locking. It seems feasible to develop a fully semiclassical description in terms of Landau-Zener theory. The $\{\alpha\}_{4,5,6,7}$ multiplet is a natural candidate for such an approach. This will be discussed in another paper.[40] The energy dependence of cross sections deserves more scrutiny than it has received here. We are in the process of perfecting a time-of-flight measurement technique, employing a pseudorandom laser chopper.[37] When used with seeded beams, and ultimately a hollow cathode arc metastable beam source,[43] this will enable us to cover a wide energy range in considerable detail. Thus it will become much easier to correlate rate constants cited in the literature with our beam experiment results. Even in its present form, however, our crossed-beam apparatus and coupled-channel program, taken together, form an excellent test bed for interaction potentials and collision mechanisms.

[1]D. Hennecart and F. Masnou-Seeuws, J. Phys. B **18**, 657 (1985).

[2]W. Buszert, T. Bregel, R. J. Allan, M.-W. Ruf, and H. Hotop, Z. Phys. A **320**, 105 (1985); W. Buszert, T. Bregel, J. Ganz, K. Harth, A. Siegel, M.-W. Ruf, H. Hotop, and H. Morgner, J. Phys. (Paris) **46**, C1-199 (1985).

[3]M. H. Alexander, T. Orlikowski, and J. E. Straub, Phys. Rev. A **28**, 73 (1983).

[4]G. Nienhuis, Phys. Rev. A **26**, 3137 (1982).

[5]J. G. Kircz, R. Morgenstern, and G. Nienhuis, Phys. Rev. Lett. **48**, 610 (1982).

[6]H. A. J. Meyer, H. P. van der Meulen, and R. Morgenstern, Z. Phys. D **5**, 299 (1987).

[7]D. Neuschäfer, M. O. Hale, I. V. Hertel, and S. R. Leone, in *Electronic and Atomic Collisions*, edited by D. C. Lorents, W. E. Meyerhof, and J. R. Peterson (American Elsevier, New York, 1986), pp. 585–591.

[8]M. O. Hale, I. V. Hertel, and S. R. Leone, Phys. Rev. Lett. **53**, 2296 (1984); M. O. Hale and S. R. Leone, Phys. Rev. A **31**, 103 (1985).

[9]J. M. Parson and T. Ishikawa, J. Chem. Phys. **80**, 3137 (1984).

[10]A. Bähring, I. V. Hertel, E. Meyer, W. Meyer, N. Spies, and H. Schmidt, J. Phys. B **17**, 2859 (1984).

[11]D. Hennecart, J. Phys. (Paris) **39**, 1065 (1978); Thesis, Université de Caen, 1982.

[12]J. M. Mestdagh, J. Berlande, P. de Pujo, J. Cuvallier, and A. Binet, Z. Phys. A **304**, 3 (1982).

[13]E. Düren, E. Hasselbrink, and H. Tischen, Phys. Rev. Lett. **50**, 1983 (1983).

[14]L. Hüwel, J. Maier, and H. Pauly, J. Chem. Phys. **76**, 4961 (1982).

[15]H. J. Yuh and P. J. Dagdigian, Phys. Rev. A **28**, 63 (1983).

[16]N. Böwering, M. R. Bruce, and J. W. Keto, J. Chem. Phys. **84**, 709 (1986); **84**, 715 (1986).

[17]J. K. Kuh and D. W. Setser, J. Chem. Phys. **84**, 4304 (1986).

[18]I. V. Hertel, H. Schmidt, A. Bähring, and E. Meyer, Rep. Prog. Phys. **48**, 375 (1985).

[19]M. P. I. Manders, J. P. J. Driessen, H. C. W. Beijerinck, and B. J. Verhaar, Phys. Rev. Lett. **57**, 1577 (1986); **57**, 2472 (1986).

[20]M. J. Webster and M. J. Shaw, J. Phys. B **12**, 3521 (1979).

[21]F. C. M. Coolen, N. van Schaik, R. M. M. Smits, M. Prins, and L. W. G. Steenhuysen, Physica (Amsterdam) **93B&C**, 131 (1978).

[22]R. M. M. Smits, thesis, Eindhoven University of Technology, 1977.

[23]R. S. F. Chang and D. W. Setser, J. Chem. Phys. **72**, 4099 (1980).

[24]J. S. Cohen and B. Schneider, J. Chem. Phys. **61**, 3230 (1974).

[25]S. Iwata, Chem. Phys. **37**, 251 (1979).

[26]F. Masnou-Seeuws, M. Philippe, and P. Valiron, Phys. Rev. Lett. **41**, 95 (1978).

[27]P. J. Dagdigian and M. L. Campbell, Chem. Rev. **87**, 1 (1987).

[28]H. Haberland, W. Konz, and P. Oesterlin, J. Phys. B **15**, 2969 (1982).

[29]I. Dabrowski and G. Herzberg, J. Mol. Spectrosc. **73**, 183 (1978).

[30]R. B. Bernstein, *Atom Molecule Collision Theory* (Plenum, New York, 1979).

[31]A. M. Schulte, thesis, Eindhoven University of Technology, 1978.

[32]J. Raynal in *Computing as a Language of Physics*, edited by A. E. Salam (IAEA, Vienna, 1972).

[33]W. J. G. Thijssen, B. J. Verhaar, and A. M. Schulte, Phys. Rev. C **23**, 984 (1981).

[34]M. J. Verheijen, H. C. W. Beijerinck, L. H. A. M. van Moll, J. P. J. Driessen, and N. F. Verster, J. Phys. E **17**, 904 (1984).

[35]M. J. Verheijen, H. C. W. Beijerinck, and N. F. Verster, J. Phys. E **15**, 1198 (1982).

[36]H. C. W. Beijerinck and N. F. Verster, Physica C **111**, 327 (1981).

[37]M. P. I. Manders, W. M. J. Ruyten, W. B. M. van Hoek, and H. C. W. Beijerinck (unpublished).

[38]A. Messiah, Quantum Mechanics (North-Holland, Amsterdam, 1981), Vols. I and II.

[39]M. J. Verheijen, H. C. W. Beijerinck, and N. F. Verster, Rev. Sci. Instrum. **56**, 62 (1985).

[40]M. P. I. Manders, E. J. D. Vredenbregt, W. B. M. van Hoek, H. C. W. Beijerinck, and B. J. Verhaar (unpublished).

[41]P. Hartmetz and H. Schmoranzer, Phys. Lett. A **93**, 404 (1983).

[42]W. L. Wiese, M. W. Smith, and B. M. Glennon, *Atomic Transition Probabilities* Natl. Bur. Stand. Ref. Data Ser., Natl. Bur. Stand (U.S.) Circ. No. 4 (U.S. GPO, Washington, D. C., 1966), Vol. 1.

[43]P. G. A. Theeuws, H. C. W. Beijerinck, D. C. Schram, and N. F. Verster, J. Phys. E **15**, 573 (1982).